Effect of Liquid Films on the Drying of Porous Media

A. G. Yiotis and A. G. Boudouvis
Dept. of Chemical Engineering, National Technical University of Athens, Zografos 15780, Greece

A. K. Stubos
National Center for Scientific Research "Demokritos", Aghia Paraskevi 15310, Greece

I. N. Tsimpanogiannis and Y. C. Yortsos
Dept. of Chemical Engineering, University of Southern California, Los Angeles, CA 90089

DOI 10.1002/aic.10265
Published online in Wiley InterScience (www.interscience.wiley.com).

The effect is studied of capillarity-driven viscous flow through macroscopic liquid films during the isothermal drying of porous materials. A mathematical model that accounts for viscous flow in a 2-D pore network, through both the liquid films and the bulk liquid phase, is presented. The results are compared with previous works that do not account for the effect of films and with experimental findings by other authors. It is shown that film flow is a major transport mechanism in the drying of porous materials, its effect being dominant when capillarity controls the process, which is the case in typical applications. By contrast, viscous flow in the bulk contributes negligibly. The results are then generalized to drying under an applied temperature gradient. © 2004 American Institute of Chemical Engineers *AIChE J,* 50: 2721–2737, 2004
Keywords: porous media, drying, liquid films, diffusion, invasion percolation

Introduction

The drying of porous media is a displacement process, in which the liquid phase in the pore space recedes as a result of evaporation. A typical geometry in an isothermal drying application is shown in Figure 1. Drying is driven by the injection of a purge gas at one side (the open end) of the medium, all other boundaries of which are no-flow boundaries. The liquid evaporates and is transferred by diffusion and convection toward the open end, where it is purged. Capillary and viscous forces control the various liquid–gas interfaces.

The problem has been addressed in the past using mostly phenomenological approaches. In these, the porous medium is a continuum; the dependent variables, like moisture content, are volume-averaged quantities; and the relation of fluxes to gradients is through empirical coefficients. A good account of such methods can be found, for example, in the reviews by Luikov (1966) and Whitaker (1977, 1998, 1999). Effective continuum mass and energy balances are supplemented by postulated constitutive equations to provide the dependency of parameters on process variables. Although useful as effective models, the weakness of such approaches is that they often lack an understanding of the phenomena at the pore or pore-network scales.

More recent work has focused on mechanistic pore-level studies (Freitas and Prat, 2000; Laurindo and Prat, 1996, 1998a,b; Le Bray and Prat, 1999; Nowicki et al., 1992; Pan et al., 1995; Prat, 1993, 1995; also see the review by Prat, 2002). An important realization that has emerged is that, like other phase change processes in porous media (Yortsos and Stubos,

A. G. Yiotis is also affiliated with the National Center for Scientific Research "Demokritos", Aghia Paraskevi 15310, Greece.
Current address of I. N. Tsimpanogiannis: Los Alamos National Laboratory, Earth & Environmental Sciences Division (EES-6), Los Alamos, NM 87545.
Correspondence concerning this article should be addressed to Y. C. Yortsos at yortsos@usc.edu.

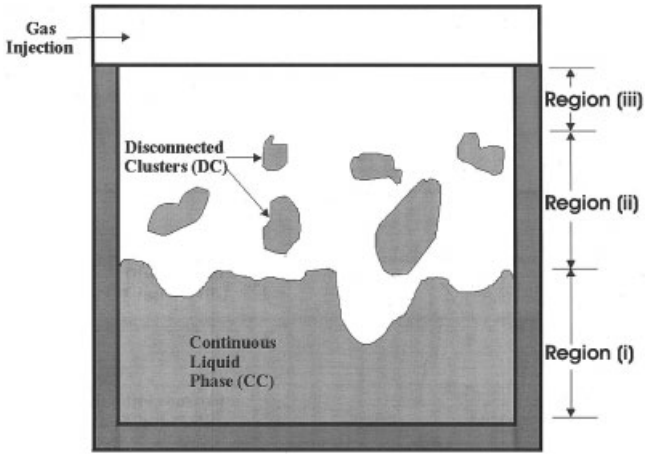

Figure 1. Drying of a liquid in a porous medium.

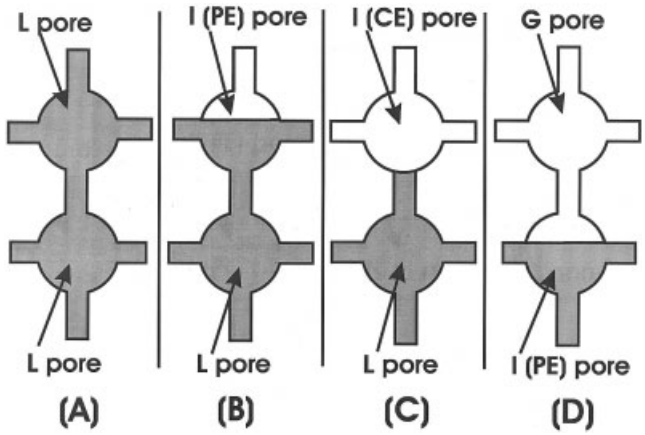

Figure 2. Typical interfaces assumed during the displacement of a meniscus, in the absence of liquid films (from Yiotis et al., 2001).

2001), drying is a drainage process, where the evaporating wetting liquid is being displaced by a nonwetting gas. Thus, in the absence of viscous effects, the pattern of the receding interface is described by invasion percolation (IP) (Lenormand and Zarcone, 1985; Wilkinson, 1986; Wilkinson and Willemsen, 1983). IP conditions apply at low drying rates (which, for example, always occur at the later stages of the process).

Compared to other drainage processes, a unique aspect of drying is the existence of disconnected clusters (DC) of the liquid [region (ii) in Figure 1], which develop in front of the main continuum liquid cluster (CC) [region (i) in Figure 1]. These act partly to screen it from the evaporating side of the porous medium. Mass transfer in the gas phase controls the rates of displacement and affects the patterns of the continuous and the disconnected clusters. When viscous effects in the gas and liquid phases are important, the drying patterns depart from IP, and the displacement can be described as invasion percolation in a stabilizing gradient (IPSG) (Prat and Bouleux, 1999; Tsimpanogiannis et al., 1999).

To understand pore-network level phenomena involved in drying, pore-network simulation methods of increasing sophistication have been used. In early efforts (Prat, 1993, 1995) the pattern of the receding interfaces, in both the DC and the CC, was assumed controlled by local percolation rules (as also discussed by Li and Yortsos, 1995, in the context of solution gas-drive), and the mass transfer in the gas by quasi-static diffusion. Effects of gravity were added by Laurindo and Prat (1996, 1998a,b). Drying rates were computed by solving the diffusion equation around the percolation interfaces of the DCs and the CC. Subsequently, viscous effects were added, in an approximate fashion, by Tsimpanogiannis et al. (1999), and using a more elaborate pore-network simulation by Yiotis et al. (2001). The latter accounts for viscous effects in the gas and in the liquid, and for advection and transients in the gas phase. Increasing the velocity of the purge gas leads to a smaller number of disconnected clusters, a smoother interface of the continuum cluster, and accelerated drying. However, these effects diminish as the drying front recedes deeper into the porous medium and the simpler picture of IP and quasi-static diffusion control reemerges. Two studies using similar concepts, but also incorporating temperature gradients, appeared recently in the literature (Huinink et al., 2002; Plourde and Prat, 2003). Temperature entered in two important properties, the interfacial tension and the equilibrium vapor pressure, and was shown to exert important effects on the patterns and the drying rates, respectively.

Common to all these works has been the absence of films. All gas–liquid interfaces were assumed in the form of menisci, spanning across a pore-throat or a pore-body cross section (for example, see Figure 2, borrowed from Yiotis et al., 2001). Such a meniscus separates a completely empty (CE) gas pore from a full liquid pore (L) (see Figure 2C). When the pressure difference across it reaches the capillary threshold of the pore, the meniscus will recede (be displaced) to an adjacent pore (Figures 2B and D). During this process, the meniscus moves across the emptying pore [which is here denoted as partly empty (PE)]. This conceptual sequence has been used by Yiotis et al. (2001) to develop a pore-network model of the process. One important aspect missing from such and related models, however, is the presence of wetting films. For example, it is well known that in realistic (not cylindrical) pore geometries, the meniscus displacement will be followed by the formation of liquid films along the pore surface (schematically shown in Figure 3). The films provide hydraulic conductivity for the receding liquid, and can play an important role in the transport of mass and, in the present context, in evaporation.

The literature on films on surfaces is immense and we will not attempt to even summarize it here, our focus being only on larger-scale phenomena of relevance to porous media. Moreover, in this work we will restrict attention to macroscopic or "thick" films. Thin films, with thickness of the order of nano-

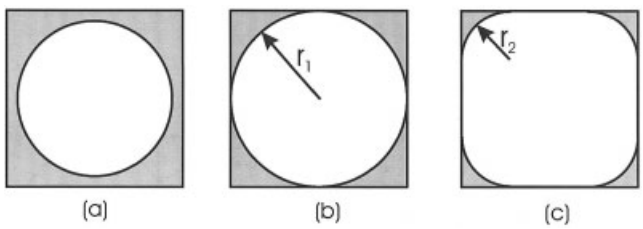

Figure 3. Evolution of film curvature in the cross section of a square throat.

meters, are certainly of interest, although their hydraulic conductivity is very low (Davis, 1996; Lenormand and Zarcone, 1984). Their relevance to porous media transport, particularly at the trailing end of drainage, has been emphasized by many authors (Davis, 1996; De Gennes, 1985a; Toledo et al., 1992). However, their contributions to the overall liquid flow in drying should be negligible compared to that of thick films.

Flow through macroscopic films has been analyzed in the context of imbibition by many authors, including Lenormand and Zarcone (1984), Lenormand (1992), Dullien et al. (1997), and Constandinides and Payatakes (2000), among others. Lenormand (1992) described in detail the expected mechanisms attributed to film flow in imbibition. During displacements in packed beds of beads of a rough surface, Dullien et al. (1997) reported flow along surface microchannels that provide hydraulic connectivity between macroscopically isolated liquid regions. This was found to be negligible in the case of smooth glass beads. Dillard and Blunt (2000) examined mass transfer from liquid films in dissolution processes, whereas Blunt et al. (2002) presented a detailed review of flow through films in the context of three-phase flow. Constandinides and Payatakes (2000) demonstrated the importance of precursor wetting films on the roughness of the pore walls, in forced imbibition at low capillary numbers.

In the context of drying, past experimental work has emphasized the existence and speculated on the role of film flow (Laurindo and Prat, 1998a; Shaw, 1987; Tsimpanogiannis et al., 1999). In a series of visualization experiments Shaw (1987) found that, under comparable conditions, the drying front in a cell containing packed beads moved one order of magnitude faster than when the cell was empty. Shaw attributed this "unorthodox" result to liquid counterflow through films that form along particle contacts, and argued that it is the dominant mechanism for the drying of porous materials. Laurindo and Prat (1998a) performed drying experiments in two-dimensional (2-D) etched-glass micromodels and compared their results with predictions from a pore-network simulator, which did not contain films. The experimental rates were found to be about sixfold higher than the numerical rates. These authors also attributed the flow enhancement to wetting liquid films and presented a simplified model for the associated transport mechanism. Liquid films were described in the form of a bundle of microcapillaries on the pore surface. However, no quantitative models for film flow were developed.

This report addresses the role of wetting films in the context of drying. The objective is to determine whether film flows can be as significant mechanism of drying as purported to be in the experiments cited. A parallel objective is to explore results that may arise from the counterflow configuration, such as where the displacement of the liquid–gas interface is in one direction, but the liquid flow in the opposite direction. We address these issues by providing a pore-network study. The basic elements of this article were reported in a previously submitted brief communication (Yiotis et al., 2003). Here, we expand on the approach used and we also consider the more general case where viscous effects in the bulk liquid are included. These were neglected previously. As a first approximation, we will neglect temperature effects. After developing the basic theory, temperature effects will be introduced. Gravity will not be considered, although its inclusion is straightforward.

The article is organized as follows. After the general formulation of the problem, we focus, first, on film flow in a long capillary, to develop useful insights for the porous medium problem. Then, we develop the basic aspects of the theory and proceed with numerical simulation. As is customary, we use a porous medium representation in terms of a pore network. Finally, we address the effect of temperature gradients. Results are analyzed and discussed.

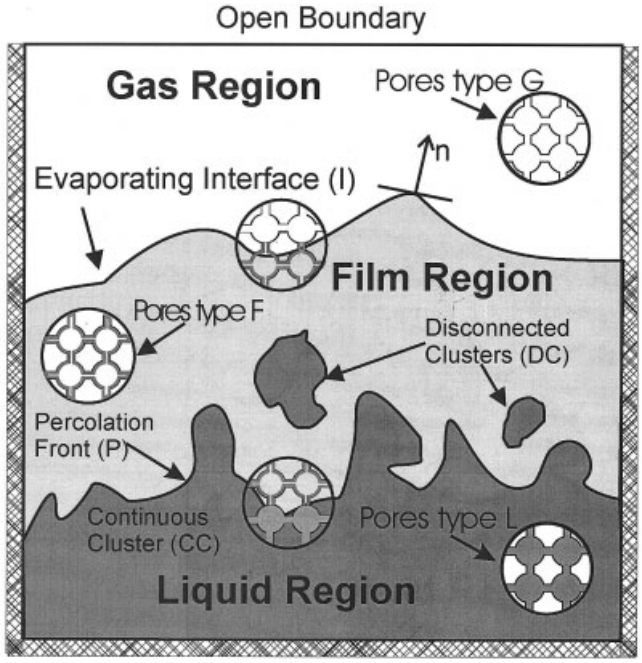

Figure 4. Liquid and gas phase patterns, indicating the various types of pores in drying used in this study.

Problem Formulation

Consider the isothermal evaporation of a single-component liquid in a porous medium (see also section on temperature effects). As shown in Figures 1 and 4, one side of the medium is open to the ambient environment, which is kept dry (through the flow of a purge gas), whereas the other three sides are impermeable to fluid flow and mass transfer. The porous medium will be represented by a 2-D square lattice of pores connected through throats with polygonal (such as a square) cross section, as shown in Figures 2–4. For simplicity, all pores are assumed to be of the same volume. However, the radii of the throats, and thus the corresponding capillary thresholds, will be distributed randomly. In the presence of films, at any stage of drying, the pore space can be characterized by three kinds of pores (Figure 4): type-L pores, fully occupied by liquid; type-G pores, fully occupied by gas; and type-F pores, occupied by gas but also containing liquid films. The existence of pores of type F is the distinguishing feature of this work, compared to previous works in drying (Laurindo and Prat, 1998a,b; Plourde and Prat, 2003; Prat, 1993; Prat and Bouleux, 1999; Tsimpanogiannis et al., 1999; Yiotis et al., 2001). Our focus is on thick films (such as those that form in the corners of polygonal pores), and where flow is driven by capillary pressure gradients. Here, we will account for viscous effects both in the films (F pores), as well as in the continuous liquid

phase (region L), which were neglected in our short communication (Yiotis et al., 2003). Mass transfer in the gas phase is assumed only by diffusion, which is usually valid in drying problems (Laurindo and Prat, 1996, 1998a,b; Prat, 1995; but see also Yiotis et al. 2001).

Because of the applied concentration gradients, the liquid evaporates along the liquid–gas interfaces, the resulting gas-phase species diffusing in the gas phase toward the dry end. During this process, the macroscopic gas–liquid interfaces (denoted by P in Figure 4) recede, both in the continuous and the discontinuous clusters. The rates and patterns under which this occurs is the ultimate objective of this work. An algorithm on how menisci recede in the absence of film flow was formulated in Yiotis et al. (2001). The goal of this work is to incorporate the effect of film flow, such as in the pores of type F, on the patterns and rates of displacement, and the rates of drying.

To proceed, we will parameterize a film in region F by its radius of curvature r, which is a function of time and distance. Assuming local capillary equilibrium at the film interface, we have

$$P_c = P_g - P_l = \frac{\gamma}{r} \tag{1}$$

where γ is the interfacial tension. By neglecting variations in the gas pressure (for an account of these effects, see Yiotis et al., 2001) we can take without loss, $P_g = 0$. Then, the pressure in the film (P_l) is

$$P_l = -\frac{\gamma}{r} \tag{2}$$

Fluid flow through the film will result in the decrease of the liquid pressure, and thus, according to Eq. 2, to a decrease of the film radius (and the film thickness). Conversely, any decrease of the film radius will induce a corresponding flow, driven by capillarity.

For further progress, we must write mass balances for the evaporating species in the film and in the gas, which must then be coupled to the full problem. Given the complexity of the pore space this is by no means a trivial task. We will show, however, that it is possible to make meaningful progress with a relatively simple approach. For this, we must consider first a single film in a long capillary.

Liquid flow through macroscopic films in a single capillary

Several authors (Lenormand and Zarcone, 1984; Ransohoff and Radke, 1988; Zhou et al., 1997) studied film flow along the corners of long smooth capillaries with polygonal cross sections. Assuming unidirectional (direction x) viscous flow, a Poiseuille-type law applies in these geometries

$$Q_x = -\frac{\alpha r^4}{\mu_l}\frac{\partial P_l}{\partial x} \tag{3}$$

where Q_x is the volumetric flow rate, α is a dimensionless geometric factor, and μ_l is the liquid viscosity. By combining Eqs. 2 and 3, we obtain

$$Q_x = -\frac{\alpha\gamma r^2}{\mu_l}\frac{\partial r}{\partial x} \tag{4}$$

Parameter α was determined previously for various model geometries (Dong and Chatzis, 1995; Ransohoff and Radke, 1988). For example, the latter authors studied film flow in one corner of a capillary with a polygonal cross section and found the following expression

$$\alpha = \frac{C^*}{\beta} \qquad \text{where}$$

$$C^* = \left[\frac{\cos\theta\cos(\pi/4+\theta)}{\sin(\pi/4)} - (\pi/4-\theta)\right] \tag{5}$$

where the shape factor C^* is expressed in terms of the contact angle θ. The dimensionless resistance β was previously calculated by Ransohoff and Radke (1988). In our case, $\theta = 0$, thus $C^* = 1 - \pi/4$ and $\beta = 93.5$; thus, in the simulations below (capillaries of square cross section), we will take $\alpha = 0.0022$. We note that this parameter is of order 10^{-3}. We also add that in the above, that the capillary and the flow conductivity radii are of the same order of magnitude, given that the pore walls are assumed smooth. In more complex film flow models, where the pore walls are rough, the two are not the same (Constantinides and Payatakes, 2000), thus affording an additional length scale, and also ensuring the stability of long films. The latter was tacitly assumed here.

Consider, now, the mass balance for the evaporating species in the capillary, by accounting for the four liquid films in the cross section. Then

$$(4-\pi)\frac{\partial r^2}{\partial t} = -4\frac{\partial Q_x}{\partial x} - Q_{ev} \tag{6}$$

where Q_{ev} is the evaporation rate. To evaluate the latter we use the simple diffusion model

$$Q_{ev} = \left(\frac{2\pi rD}{\rho_l}\right)\frac{(C_e - C)}{r_0} \tag{7}$$

where D is a measure of the gas-phase diffusivity; C is the average gas-phase mass concentration (mass per unit volume) of the evaporating species; C_e is the equilibrium concentration, a function of temperature; ρ_l is liquid density; and r_0 is the size of the capillary. We recognize that the particular details of film evaporation, particularly near the tip of the film, are very complex, involving precursor films, instabilities, and the interplay between disjoining pressures, thin films, decreasing vapor pressure as a result of Kelvin effects, and heat and mass transfer (Cazabat et al., 1990; De Gennes, 1985b; Derjaguin et al. 1987; Kataoka and Troian, 1997; Oron et al., 1997; Peterson, 1994; Wayner, 1991, 1999). Clearly, then, Eq. 7 is only a first-order approximation, and the value of D is a lumped

parameter to account for many of these omissions. Although we understand these limitations, our goal is to provide a leading-order description of the problem at the larger scale, which involves several pore radii, and it is with this understanding that we will proceed. Combining Eqs. 4, 6, and 7 then leads to

$$\frac{\partial r}{\partial t} = \frac{2\alpha\gamma}{(4-\pi)\mu_l}\left[r\frac{\partial^2 r}{\partial x^2} + 2\left(\frac{\partial r}{\partial x}\right)^2\right] - \frac{\pi D}{(4-\pi)\rho_l}\frac{(C_e - C)}{r_0} \quad (8)$$

For dimensionless notation, we introduce the diffusive time $\tau = Dt/r_0^2$, a rescaled radius of curvature $\rho = r/r_0$, a rescaled axial distance $\xi = x/r_0$, and a dimensionless concentration $\zeta = C/C_e$, based on which we write

$$\left[\frac{(4-\pi)\rho_l}{\pi C_e}\right]\mathrm{Ca}\frac{\partial \rho}{\partial \tau} = \rho\frac{\partial^2 \rho}{\partial \xi^2} + 2\left(\frac{\partial \rho}{\partial \xi}\right)^2 + \mathrm{Ca}(\zeta - 1) \quad (9)$$

Here we introduced the capillary number $\mathrm{Ca} = \pi D C_e \mu_l / 2\alpha\rho_l r_0 \gamma$. As in other mass-transfer driven processes (for example, Satik et al., 1995), this capillary number expresses the ratio of the viscous forces attributed to flow driven by mass transfer to capillary forces.

Equation 9 is coupled to the mass balance in the gas phase. Proceeding in a similar fashion we find

$$\frac{\partial C}{\partial t} = D\frac{\partial^2 C}{\partial x^2} + \frac{1}{2}\frac{\pi r D}{r_0^3}(C_e - C) \quad (10)$$

or, in dimensionless notation

$$\frac{\partial \zeta}{\partial \tau} = \frac{\partial^2 \zeta}{\partial \xi^2} + \frac{1}{2}\pi\rho(1-\zeta) \quad (11)$$

Equations 9 and 11 are to be solved subject to appropriate initial and boundary conditions. Before we proceed with a specific problem, however, the following remarks are in order.

(1) Given a constant supply of liquid at one end, the two equations ultimately reach a steady state. Concentration profiles reach this state in a few units of the time to diffuse over a distance of the order of a pore radius. The characteristic time for the film thickness profile to reach steady state is different, and equals the capillary time $[(4-\pi)\mu_l r_0]/2\alpha\gamma$. Of importance to our work is the comparison of these times with the time t_p it takes to empty a pore of volume at the origin of the film (where the evaporating liquid is supplied). Assuming that the driving flux is attributed to a concentration gradient $C_e/(Xr_0)$, then $t_p = \rho_l V_p X/r_0 D C_e$. Hence, for a steady state to be established before any significant movement of the origin of the film, it is required that

$$\frac{r_0^3 C_e}{V_p \rho_l} \ll X \quad (12a)$$

for the concentration and

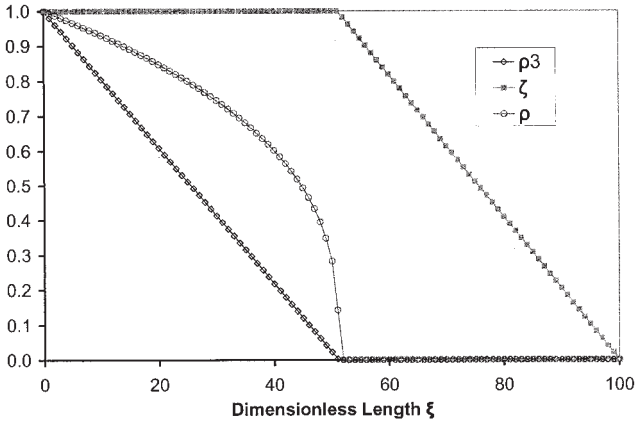

Figure 5. Steady-state profiles of the rescaled liquid film thickness and the gas phase concentration, for evaporation and film flow in a single capillary.

Ca = 0.5, N = 100.

$$\left(\frac{r_0^3}{V_p}\right)\frac{(4-\pi)\mathrm{Ca}}{\pi} \ll X \quad (12b)$$

for the film thickness. Given the large difference in the densities between the gas and the liquid phases, both these conditions are readily satisfied, even for values of the capillary number of order 1.

(2) Equation 11 suggests that the concentration follows an exponential decay, within a region of the order of a few film radii, near the end of the film. Therefore, we also infer that evaporation practically occurs near the tip of the film (in a region of the order of several film radii) and that the concentration varies mostly in that region. A numerical demonstration of both these assertions is given in Appendix A.

The development of a quasi–steady state is expected. It is consistent with other diffusion-controlled problems in porous media (for example, Peitgen and Saupe, 1988; Witten and Sanders, 1981). The restriction of the evaporation to a narrow region is a consequence of the exponential decay of the concentration: because of the confined pore geometry, the gas phase becomes rapidly saturated, limiting evaporation to a narrow region near the film tips, where the liquid flux is supplied by capillarity-driven film flow.

Figure 5 shows a typical steady-state profile obtained from the solution of Eqs. 9 and 11. The liquid flux through the film exactly balances the evaporation rate. As expected, evaporation occurs near the tip of the film, located approximately at the distance $\xi_p = N/[1 + (6\mathrm{Ca}/\pi)]$, where N is the (dimensionless) length (aspect ratio) of the capillary. To the left, the gas is saturated, and the cube of the thickness of the film is to a good approximation a linear function of distance $\rho^3 = 1 - \{6\mathrm{Ca}/[\pi(N - \xi_p)]\}\xi$. To the right, the film thickness is almost zero and the concentration profile approximately linear, as expected from the above analysis. Two-dimensional analogues will be described later.

Drying through macroscopic films in a pore network

The single-capillary physics described above are also expected to apply to the general problem, where films exist in a

network of capillaries (pores). Therefore, we will proceed and simplify the full problem in pores of the types F and G (Figure 4), by assuming the following: quasi–steady state in the film thickness, a saturated gas phase ($C = C_e$), and only film flow in F-type pores; a quasi–steady state in the concentration in G-type pores; and evaporation occurring where the films terminate, that is, at the interface I between pores F and G. Based on these assumptions, we then have the following description:

In Region F

$$\nabla^2\rho^3 = 0 \qquad \text{and} \qquad \zeta = 1 \tag{13}$$

where ρ now stands for an appropriately volume-averaged thickness.

In Region G

$$\nabla^2\zeta = 0 \qquad \text{and} \qquad \rho = 0 \tag{14}$$

Across the Evaporation Interface I

$$\frac{1}{\text{Ca}}\frac{\partial\rho^3}{\partial n} = \frac{\partial\zeta}{\partial n} \qquad \text{and} \qquad \rho = 0,\ \zeta = 1 \tag{15}$$

Equation 15 expresses the continuity of flux at the evaporation interface. Drying is driven by imposing $\zeta = 0$ at the open end of the domain (Figure 1). In Eqs. 13–15 above, we provided an upscaled version of the problem. This was done only for the sake of convenience in notation, however. In the simulations shown later, the discrete form (as appropriate for the specific pore network) is used.

We summarize the approach to be taken for modeling the effect of films: at any given time evaporation occurs only at the film tips (interface I), at rates dictated by the solution of Eqs. 13 and 14 in their respective domains, coupled with condition 15 at their interface and constrained by the conditions $\zeta = 0$ at the open end and by specifying the value of ρ at the boundary P of the liquid clusters. During the process, some liquid clusters of finite size may become disconnected and macroscopically isolated (Figures 1 and 4). The rate by which the size of a given cluster is reduced is dictated by the total rate draining the cluster through film flow. Now, if viscous forces are negligible in the bulk liquid, the location of interface P can be obtained using IP in a straightforward manner: Given a pore-network representation and pore-throat size distributions, the interface patterns of all liquid clusters correspond to invasion percolation. It is obtained recursively by invading at every invasion step the neighboring pore throat with the largest radius. This is a consequence of the fact that, in the absence of viscous effects, P_l is spatially uniform in the liquid clusters. This was the approach taken in Yiotis et al. (2003). However, neglecting viscous effects in the bulk, while retaining them in the films, is strictly speaking inconsistent. For this reason, viscous effects in both the films and the bulk liquid clusters will be considered. It is well known that in the case of external displacements, viscous effects are important, both in the displacement patterns and in the recovery rates. Whether this is also true in the case of drying will be explored in this work.

A Useful Transformation for Determining the Film Profile. Given that the location of interface I is unknown, solving the drying problem in the presence of films appears quite daunting, at first glance. Closer inspection, however, reveals that a useful transformation can be applied that leads to a rather straightforward solution. First, note that ρ^3 and ζ satisfy the Laplace equation in their respective, and mutually exclusive, domains F and G (and where ζ and ρ^3 are, respectively, constant). In addition, at interface I, the normal fluxes of ρ^3 and ζ are linearly related through Eq. 15. It follows then, that the linear combination

$$\Phi \equiv \frac{\rho^3 + \zeta\text{Ca}}{1 + \text{Ca}} \tag{16}$$

satisfies the Laplace equation *everywhere* (in both regions F and G), while remaining continuous and with continuous derivatives, also *everywhere* (including interface I). Thus, it suffices to solve the Laplace equation for Φ in the domain F + G, subject to the boundary conditions

$$\Phi \equiv \frac{\rho_i^3 + \text{Ca}}{1 + \text{Ca}} \tag{17}$$

at the liquid cluster perimeter P and to $\Phi = 0$ at the open end.

In Eq. 17, ρ_i refers to the normalized film radius of curvature at the place where the films emanate. Determining its value will be discussed further below. For the moment, we will proceed by making the approximation that the film thickness at the liquid cluster interface is approximately constant and equal to the throat radius, r_c, corresponding to the percolation threshold. This assumption has the important benefit that the boundary condition becomes decoupled from the capillary number. By taking r_c as the characteristic length scale, we have $\rho_i \approx 1$, and Eq. 17 reads $\Phi = 1$. In doing so, we implicitly assumed that the liquid cluster interfaces have the IP geometry. The validity of this approximation is explored further in Appendix B. Note also that r_c is determined from the condition $\int_{r_c}^{\infty} f(r)dr = p_c$, where p_c is the bond percolation threshold, and $f(r)$ is the pore-throat size distribution. For a square lattice, where $p_c = 0.5$, and assuming a uniform size distribution for $f(r)$, as done below, the value of r_c coincides with the arithmetic mean.

Using the above transformation, the solution of the Laplace equation can be used to determine the profiles of the film radius and the concentration, the rates of drying through each film, as well as the location of the interface I, where the films terminate and evaporation occurs. Interface I is located simply as the position where

$$\Phi = \frac{\text{Ca}}{\text{Ca} + 1} \tag{18}$$

It follows that for low values of Ca, as is typically the case, the films extend all the way to the open boundary (where $\Phi = 0$). By contrast, when Ca is of order 1, the films are short and the film tips (evaporation interface I) reside closer to the liquid cluster interface P (where $\Phi = 1$). For example, this would correspond to cases with low interfacial tensions.

In summary, given the location of interface P (that is, that of CC and DCs), we can evaluate the film radius, the concentra-

tion, and the flow rates at any point, by solving the following boundary value problems

$$\nabla^2\Phi = 0 \qquad \text{in regions G and F} \tag{19}$$

$$\Phi = 1 \qquad \text{at P} \tag{20}$$

$$\Phi = 0 \qquad \text{at the open end of the network} \tag{21}$$

In Yiotis et al. (2003) we adopted invasion percolation rules, in which case the determination of P is straightforward. In the general case, however, viscous effects in the bulk liquid may not necessarily be negligible and must be accounted for. For this, we will proceed as follows.

Liquid Cluster Patterns and their Perimeter P. In all pores occupied fully by liquid (pores of type L), the viscous flow is described by Poiseuille-type expressions. For such pores, the liquid mass balance at any pore i reads in dimensionless notation as

$$\sum_j (p_i - p_j)\sigma_{ij}^4 = 0 \tag{22}$$

where j denotes a neighboring pore, σ is dimensionless pore radius, and we have normalized pressure drops with the characteristic value $P^* = \gamma/r_c$. For pores at the perimeter P, however, the mass balance is different and we need to further distinguish two cases.

If the liquid pressure at a perimeter pore is not sufficiently small, for the gas in the neighboring pore (CE in Figure 2) to penetrate the connecting throat, the meniscus remains stationary. Because of the films, however, there is always net liquid outflow from the pore. The corresponding mass sink is calculated by the film flow solution discussed earlier, using the Laplace equation. In dimensionless notation, the mass balance is then

$$-\sum \left.\frac{\partial p}{\partial \xi}\right|_P \sigma_{ij}^4 = \sum_j (p_P - p_j)\sigma_{ij}^4 = -\frac{32\alpha}{3\pi}(1 + \mathrm{Ca}) \sum_F \left.\frac{\partial \Phi}{\partial \xi}\right|_P \tag{23}$$

where the first and second sums denote the liquid arriving at the perimeter pore P and the last sum denotes the contributions from the films in pores of type F draining the perimeter pore.

If the capillary pressure at a perimeter throat is sufficiently high, that is, if the following condition is satisfied

$$-p_P > \frac{1}{\sigma_{ij}} \tag{24}$$

the adjacent pore is penetrated, thus becoming partly empty (PE) (Figure 2), and leading to bulk-liquid displacement. As in Yiotis et al. (2001), in such pores we assume that the capillary pressure is zero. The latter is certainly an assumption. Strictly speaking, one needs to follow in detail the local curvature, given that it results from the calculation of the viscous pressure fields. However, at least in this report, where viscous effects on the patterns will turn out to be very small for typical values, the error of this assumption is not significant. Then, the corresponding mass balance reads in dimensionless notation

$$\sum_j \left.\frac{\partial p}{\partial \xi}\right|_P \sigma_{ij}^4 - \frac{32\alpha}{3\pi}(1 + \mathrm{Ca}) \sum_F \left.\frac{\partial \Phi}{\partial \xi}\right|_P = \sum_j p_j \sigma_{ij}^4 - \frac{32\alpha}{3\pi}(1 + \mathrm{Ca}) \sum_F \left.\frac{\partial \Phi}{\partial \xi}\right|_P = \frac{8\mu_l Q_P}{\pi r_0^2 \gamma} \equiv (1 + \mathrm{Ca}) q_P \tag{25}$$

where we have taken $p_P = 0$. The righthand side in Eq. 25 is the volume flow rate at which the perimeter pore P empties, and q_p is a dimensionless flow rate. Then, the gas volumetric fraction (saturation, S) of such a pore increases in time as

$$\Delta S_i = \frac{\Delta t}{V_p} Q_P = q_p \Delta \tau \tag{26}$$

where Q_P is assumed constant during the time step and we made time dimensionless using the characteristic time $t^* = 8V_p\mu_l/[\pi r_c^2 \gamma(1 + \mathrm{Ca})]$. This time is a multiple of the diffusion time defined earlier for the single capillary, by the factor $16\alpha V_p \rho_l \mathrm{Ca}/[\pi^2 r_c^3 C_e(1 + \mathrm{Ca})]$. For future use, we can also write

$$t^* = \left(\frac{16\alpha}{\pi^2}\right)\left(\frac{V_p \rho_l}{r_c D C_e}\right)\left(\frac{\mathrm{Ca}}{1 + \mathrm{Ca}}\right)$$

an expression that will be used extensively below.

We now have the relevant information to determine the solution of the full problem. Before we proceed, we note that in addition to the pore-size distribution, the other two dimensionless parameters that enter in the problem are the viscous conductivity parameter α and the capillary number Ca. In fact, the effect of Ca enters only in the combination $(1 + \mathrm{Ca})$ (see Eqs. 23 and 25). This means that for viscous forces to have a noticeable effect on drying *patterns* (thus the dimensionless drying rates), the capillary number must be of *order 1*. Thus, before we even solve the full problem, we anticipate that the patterns of the liquid clusters would be of the IP type, provided that Ca is less than of order 1, but not necessarily very small (and provided that the liquid clusters are not very close to the open end, where the gradients

$$\sum_F \left.\frac{\partial \Phi}{\partial \xi}\right|_P$$

can be large). This is typically the case. The remark also validates the assumption we made on the constant film thickness at the liquid cluster perimeter. Although a significant effect on the pattern requires capillary numbers of the order of 1, however, the effect of the capillary number on the *dimensional* drying rates is significant, and enters when the capillary numbers are small, as will be shown below. It is worth contrasting this behavior to the case of external injection, such as in forced drainage, where viscous effects on the pattern start becoming important for much lower values of the capillary number (such as of the order of 10^{-3}) (Chatzis et al., 1983; Larson et al., 1977; Xu et al., 1998), or for even lower values

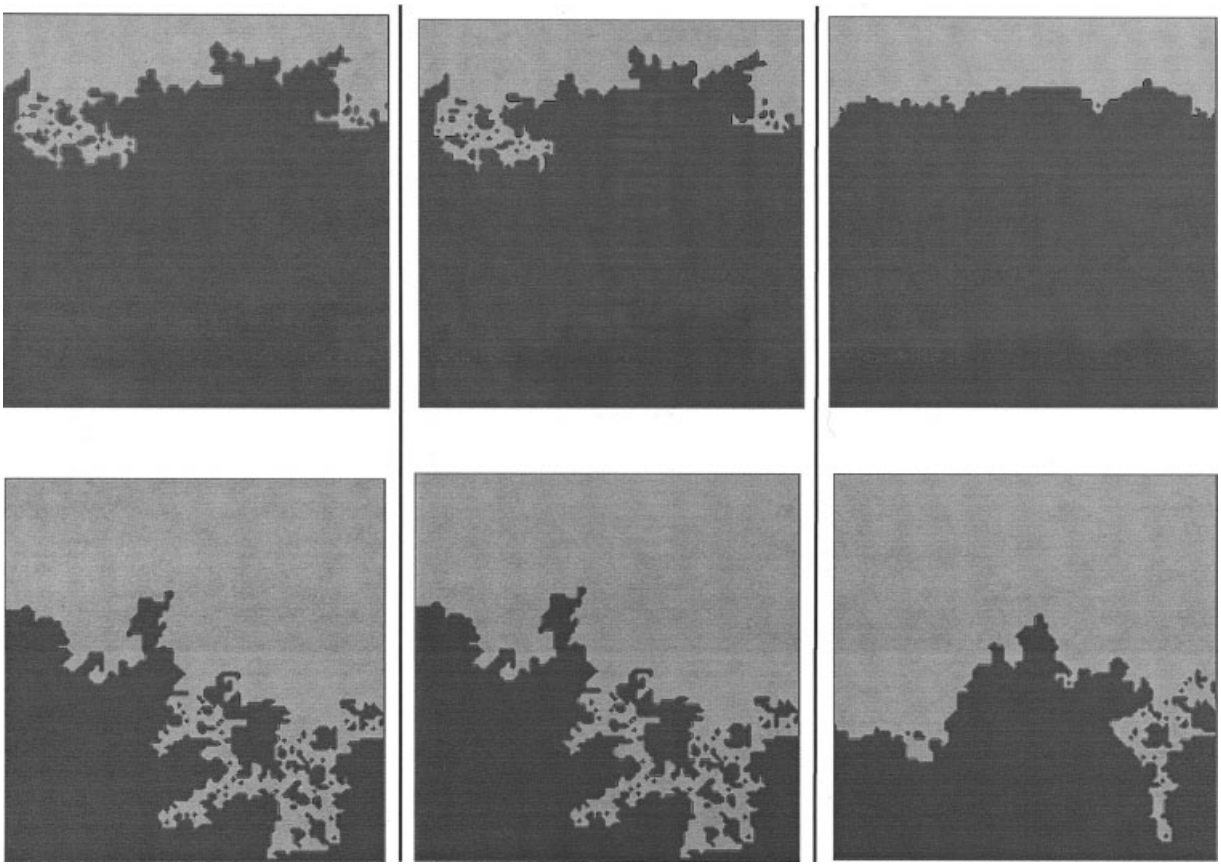

Figure 6. Two snapshots of the drying front for Ca = 10^{-4} (left), Ca = 1 (middle), and Ca = 10 (right).

Liquid-occupied pores are in black.

of the order of 10^{-6} (Dias and Payatakes, 1986; Vizika and Payatakes, 1988). This difference reflects the characteristic of countercurrent flow in drying, which is absent from external displacements.

Numerical Results and Discussion

We proceed next to solve the problem numerically. The simulation in the network, the updating of interfaces and the marching in time is similar to that in Yiotis et al. (2001), and will be qualitatively summarized as follows. At any given time, pores have one of the designations L, F, or G (Figure 4). The L pores can be part of the original liquid cluster (CC) or of the disconnected finite-size clusters (DC). At every new time step, the overall rate of evaporation from each of the liquid clusters is evaluated using the Laplace equation. Pressure fields in the liquid clusters are calculated and PE pores are emptied according to the appropriate mass balances described above. The time step is selected such that it equals the minimum time required to empty completely any of the available PE pores. If at the current time no PE pores are available to any (or all) of the clusters (that is, if all pores are of the CE type), the throat with the smallest capillary threshold in the perimeter of any given cluster is invaded next, at which time the invaded pore becomes of the PE type. To determine this throat, the liquid pressure is lowered uniformly in space inside the cluster, until the capillary pressure exceeds for the first time the smallest capillary threshold. Invasion must occur, given that, as a result of evaporation, there is a continuous loss of mass from the liquid clusters through film flow. Then, the interfaces are updated, the equation for Φ is solved again, the rates of flow through the film are obtained, and the process continues. All calculations are done explicitly in time. The fields for the pressure and Φ are computed using successive overrelaxation.

Geometric parameters include the number of pores in the linear dimension $N = L/l$, where l is the typical lattice length, the size distribution, parameter α, and the aspect ratio of the porous medium block. Herein, all geometric parameters are fixed, the throat-size distribution is taken to be uniform and preassigned on the lattice, and the aspect ratio of the matrix block is equal to 1. Emphasis is placed on the effect of the capillary number. The numerical simulations were conducted in 100×100 pore networks. We present numerical results of the patterns of the liquid clusters, the extent of the film region, and the drying rates.

Patterns

As noted above, because the pressure gradient at the front scales as (1 + Ca), the effect of the capillary number on the pattern is expected to be negligible for values of the capillary number less than order of 1. In that range, we expect that the phase distribution patterns will follow IP rules. The left panel in Figure 6 shows two snapshots of the drying front for Ca = 10^{-4}. As expected, it corresponds to an IP pattern. We note the development of many disconnected clusters, particularly at the

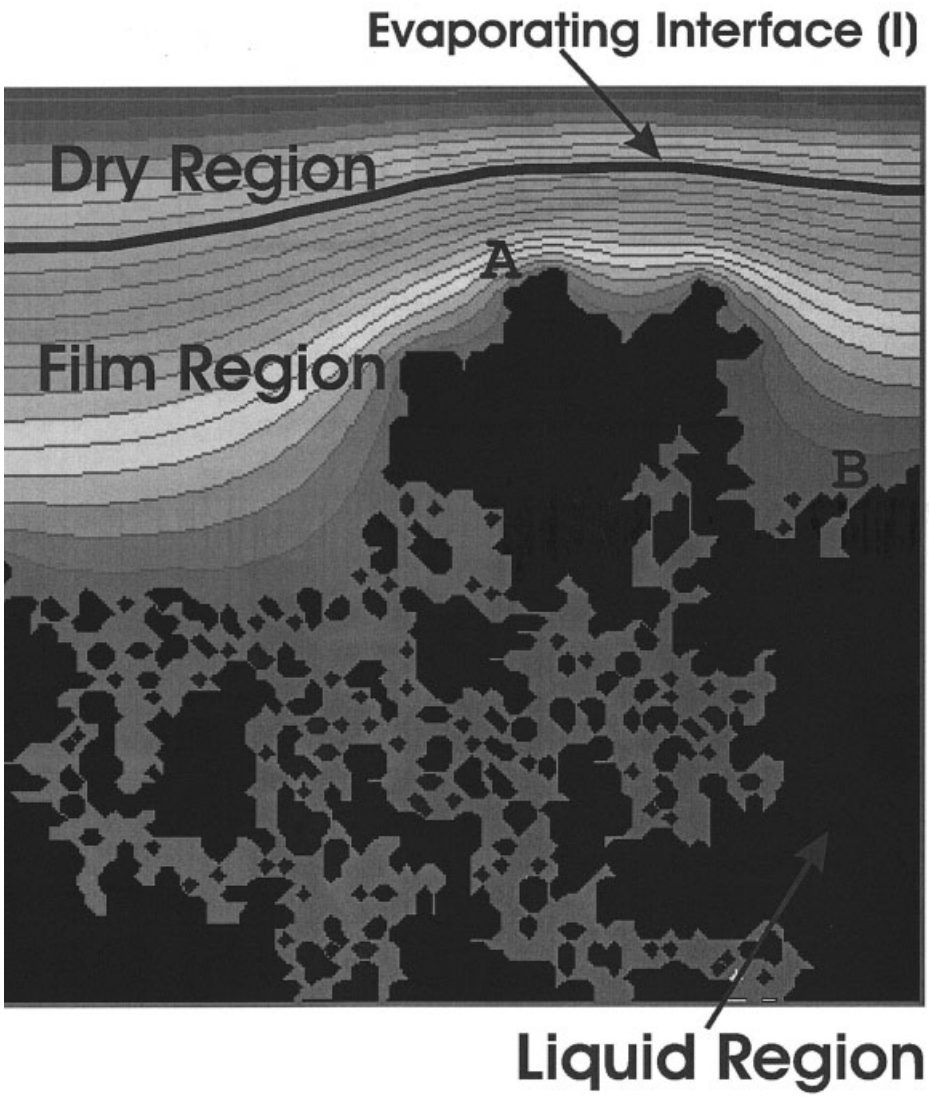

Figure 7. Isocontours of the solution of the Laplace equation around the liquid clusters, for Ca = 0.5, with boundary conditions $\Phi = 1$ at the front and $\Phi = 0$ at the open end.

later stages of the process, also as expected. Such patterns are identical to those produced in the absence of films (for example, as in Yiotis et al., 2001), although the rates by which they recede are not (see below). As the capillary number increases, the patterns will eventually depart from IP, particularly at the early times of the process. However, Figure 6 shows that quite large capillary number values are needed for a noticeable effect on the pattern. For example, the middle panel of Figure 6 shows that even for Ca = 1 the pattern is almost identical to IP, except for a few small differences at the start of the process. It takes larger values, of the order of Ca = 10 (right panel of Figure 6), for the effect to be pronounced. Then, the pressure drop at the front becomes relatively significant, and the pattern exhibits the expected behavior of viscous "stabilization" [described in Tsimpanogiannis et al., 1999, as invasion percolation in a stabilizing gradient (IPSG)]. As drying progresses, the recovery rate diminishes as a result of the receding of the percolation front. In the case of large Ca, this results to a transition from IPSG patterns to capillary-dominated IP patterns. It follows, therefore, that under typical conditions and for all practical purposes, the drying front can be accurately described as an IP front. It was noted that this is in contrast to the behavior of external drainage, where viscous effects on the pattern become important for values of the capillary number as low as 10^{-3}.

Film profiles

The film properties and the film profile are determined from the solution of the Laplace equation for Φ. Figure 7 shows a snapshot of the isopotential contours for IP patterns. (For a video of the evolution of these contours, see http://users.ntua.gr/yiotis/films.html.) These reflect the solution of the Laplace equation around a fractal object, thus following the fractal features at distances close to it, but becoming smooth at a small distance away. Because of the assumed boundary condition $\Phi = 1$ at the cluster perimeter, all clusters act as sinks, and thus there is no fluid flow from one cluster to another (see Appendix B).

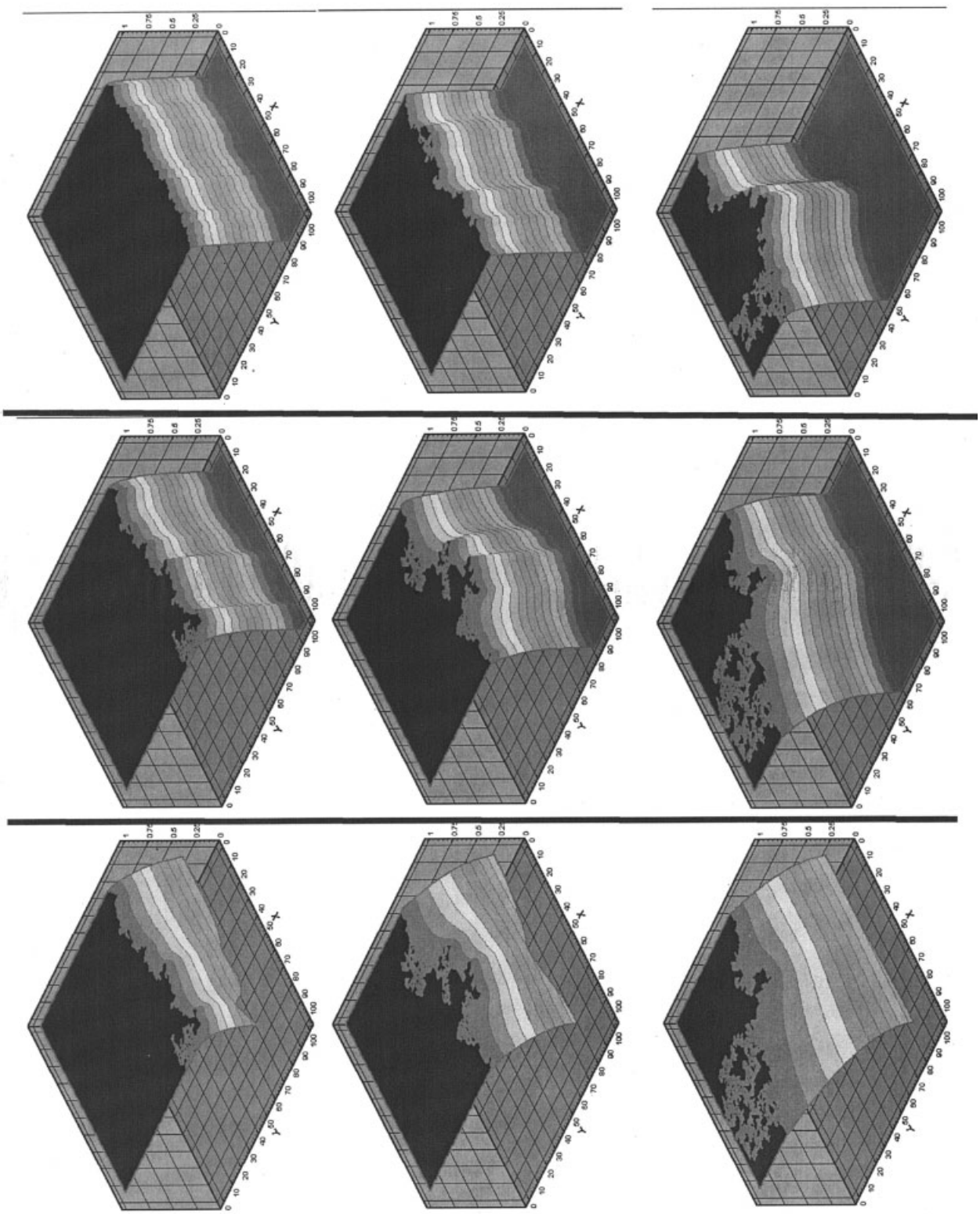

Figure 8. Profiles of the rescaled film radii for Ca = 10^{-4} (left), Ca = 1 (middle), and Ca = 10 (right) at three different stages of the process.
Liquid clusters are in black; the fully dry region is in dark gray.

Figure 8 shows normalized film radius profiles, corresponding to the same capillary numbers as in Figure 6 and at three different stages of the process. The film radius has the approximate profile $\rho \propto \xi^{1/3}$, where ξ is the distance from the front, and which corresponds to the solution of the 1-D Laplace equation, as discussed above. The location of the film tips (interface I) is the contour with the value $\Phi = \mathrm{Ca}/(\mathrm{Ca} + 1)$. It follows that the film extent increases, that is, as the value of (Ca + 1)/Ca decreases. At smaller Ca, capillarity helps to transport liquid over larger distances and to keep the film extent larger. This is favored by larger interfacial tension, larger values of r_c, and smaller viscosity and effective diffusivity. As noted, in our model, the latter is in general a lumped parameter, and may include, in addition to molecular diffusivity, various mechanisms at the film tip (Cazabat et al., 1990; Kataoka and Troian, 1997; Oron et al., 1997), which were neglected here. It certainly should include end effects, when the film tips reach all the way to the open end and which were also not accounted here.

Figure 8 shows that at low Ca (left panel), the films extend all the way to the open end, which is the place where practically all evaporation occurs. When Ca is of order 1 or larger, however, the films are shorter (middle and right panels in Figure 8), and lead to the formation of a completely dry region G, the extent of which increases with time. Even though the film region is short and a fully dry region has developed, the drying front is still of the IP type (as in the left panel). In the $O(1)$ case, the film tips mimic the protuberances of the drying front, being closer to the open boundary if associated with a corresponding protuberance. Films that end at such points will have a larger drying rate because the gradient of Φ (and of the concentration) there is larger.

Drying curves

Based on the previous notation and assuming a 2-D geometry, the overall drying rate in mass/time is expressed as

$$\Im = \frac{\phi W D l C_e (1 + \mathrm{Ca})}{\mathrm{Ca}} \Im_D \tag{27}$$

where ϕ is porosity, W is the dimensionless width of the open end (later taken as 1), $\Im_D = -\int_{a_0} (\partial\Phi/\partial n) da$ is the dimensionless drying rate, and subscript 0 denotes the open boundary. The dimensionless rate $\Im_D$ depends on the geometry of the porous medium, time, and the capillary number in the combination (1 + Ca). In dimensionless notation, the dimensionless time increment to fill one pore is

$$\Delta\tau = -\left(\frac{\pi^2 r_c}{16\alpha l \phi}\right) \frac{1}{\displaystyle\int_{a_0} \frac{\partial\Phi}{\partial n} da} \tag{28}$$

which is inversely proportional to the dimensionless rate. The dimensionless time τ can be obtained by the integration of Eq. 28.

Figure 9 shows a plot of the dimensionless drying rate $\Im_D$ as a function of the dimensionless time τ for different values of Ca. Figure 10 has the corresponding plots for the drying curves (the gas saturation of the porous medium). It is clear that the effect of the capillary number is small, and that all curves are confined in a rather narrow region, even for large (and unrealistic) values of Ca. All curves approach ultimately the high-Ca limit scaling $\Im_D \propto \tau^{-0.5}$. Thus, in contrast to the interface patterns, where the capillary number ultimately has an effect, albeit at relatively large values, drying rates and curves are practically unaffected by Ca. This is a consequence of film flow effects, which dominate the process and "regularize" the effect of the pattern, whether of the IP type or the more pistonlike displacement obtained at low capillary numbers. This "regularization" is evident in the film profiles in Figure 8.

On the other hand, the effect of the capillary number is very significant, when the drying curve is plotted as a function of *dimensional* time. Indeed, because the characteristic time was defined as

$$t^* = \left(\frac{16\alpha}{\pi^2}\right)\left(\frac{V_p \rho_l}{r_c D C_e}\right)\left(\frac{\mathrm{Ca}}{1 + \mathrm{Ca}}\right)$$

it is clear that in dimensional time, the drying process accelerates in proportion to the ratio (1 + Ca)/Ca, which in the range of realistic values is inversely proportional to Ca. We stress that this is a result of the wicking action of the films and not of increased film surface area, given that evaporation is practically restricted to the film tips. Rather, at smaller Ca, capillarity transports liquid over larger distances, leading to steeper concentration gradients because the film tips (and interface I) are closer to the open boundary, and thus to larger evaporation rates. It is readily shown that in the region of small Ca, the drying rate scales as

$$\Im \sim \frac{\gamma r_c}{\mu_l} \tag{29}$$

showing the dominant effect of capillarity in this region. Conversely, at large Ca of order 1, the film extent is smaller, films do not contribute substantially, and the drying rates are smaller. There we have, roughly,

$$\Im \sim D r_c C_e \tag{30}$$

All previous pore-network models (Laurindo and Prat, 1998a,b; Prat, 1995; Prat and Bouleux, 1999; Yiotis et al., 2001) correspond effectively to such condition.

In summary, in the typical problem, where the capillary numbers is generally less than $O(1)$, we anticipate the existence of long films that drain liquid through the above "wicking" action, and all the way to the open end where it subsequently evaporates. For instance, in the experiments in Laurindo and Prat (1998a) we have made the rough estimate Ca $\sim 10^{-4}$, suggesting that liquid films (region F) likely existed in all gas-invaded pores in the experiments and that a completely dry region (region G) did not develop. Quantitative results for the drying rate and the extent of drying in terms of a dimensional time can be obtained, such as by shifting the log τ axis in Figures 9 and 10 by log t^* (which at low Ca is equal to log Ca). It follows that an order-of-magnitude decrease in Ca will lead to an order-of-magnitude decrease in time and a corresponding

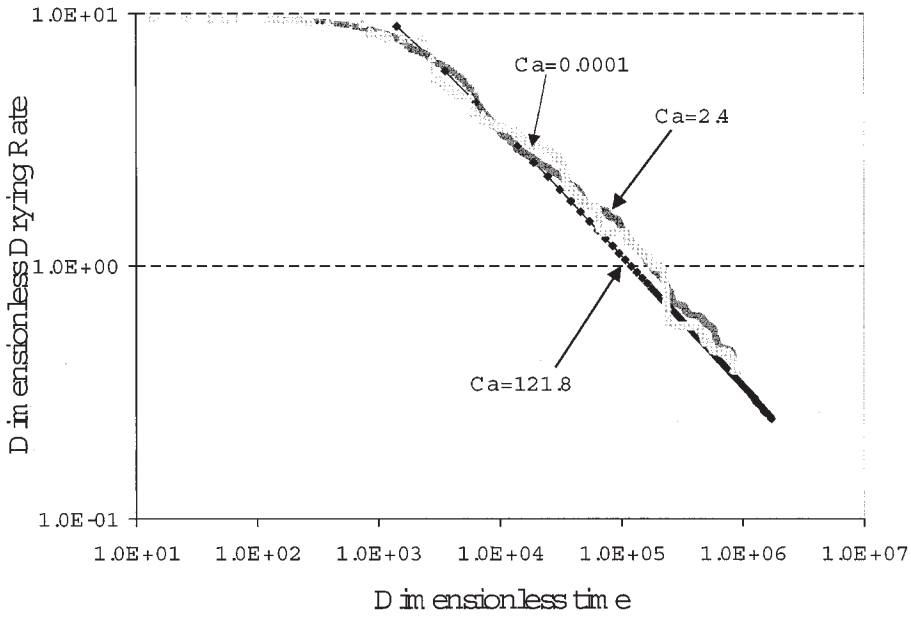

Figure 9. Dimensionless drying rate as a function of the dimensionless time, for three different values of the capillary number.

The large-Ca limit coincides with the expected scaling behavior $t^{-0.5}$.

order-of-magnitude increase in the drying rate. These are attributed exclusively to the effects of film flow.

Effect of Temperature Gradients

Temperature effects on drying processes in the absence of films were addressed recently in two studies by Prat and coworkers (Huinink et al., 2002; Plourde and Prat, 2003). Two different effects were studied, the dependency on temperature of surface tension and that of the equilibrium vapor pressure. The sensitivity of the first is important in the case of porous media of weak disorder. Then, the dependency of surface tension on temperature can lead to either stabilizing or destabilizing drying fronts, in an effect similar to gravity, depending on the direction of the application of the temperature difference. For strongly disordered porous media, however, the variation of the equilibrium vapor pressure with temperature is the more dominant effect, by accelerating the drying process.

In the presence of films, both effects will be present. However, we will restrict the present discussion to the effect of the vapor pressure only, under the assumption that the porous media disorder overwhelms the variability because of the surface tension dependency on temperature. Our emphasis, by way of reminder, is on the large scale, and in this context, small-scale instabilities ascribed to temperature will be ignored.

Isothermal effects

It is instructive to first briefly discuss temperature effects under isothermal conditions. The previous formulation suggests that elevated temperatures will affect the rates (through the dependency of C_e) only in proportion to (1 + Ca). Thus, as long as the capillary number remains low, improvements attributed to heating will be negligible, given that the film action is effective and dominates the process. However, when the capillary number is sufficiently large, then film action becomes ineffective, a scaling of the type in Eq. 30 will set in, and the process approaches the case examined in detail by Huinink et al. (2002).

Nonisothermal effects

Consider, now, the case of nonisothermal conditions. We assume that a constant temperature gradient is applied and maintained, for example, because of the dominant contribution of solid matrix conduction. This is the same assumption used in Huinink et al. (2002). The result is a corresponding gradient in the equilibrium vapor concentration, which for simplicity we will take to be a linear function of position in the same direction as the temperature gradient, that is, $C_e = Ax + C_0$,where C_0 is the reference equilibrium value. After normalizing with C_0, we thus have

$$\zeta_e = 1 + \frac{A}{C_0} x \tag{31}$$

where x is measured from the closed end. Constant A expresses the strength of the applied spatial dependency, $A \approx (dC_e/dT)(\partial T/\partial x)$. As in the isothermal case, the film region will be saturated, but now with a spatially variable equilibrium concentration. To proceed we will adopt the previous approach; that is, we will assume that for sufficiently small A, evaporation practically occurs near the evaporation interface, in which case the previous description applies, as described below.

In the film region F, the concentration is approximately equal to equilibrium, thus

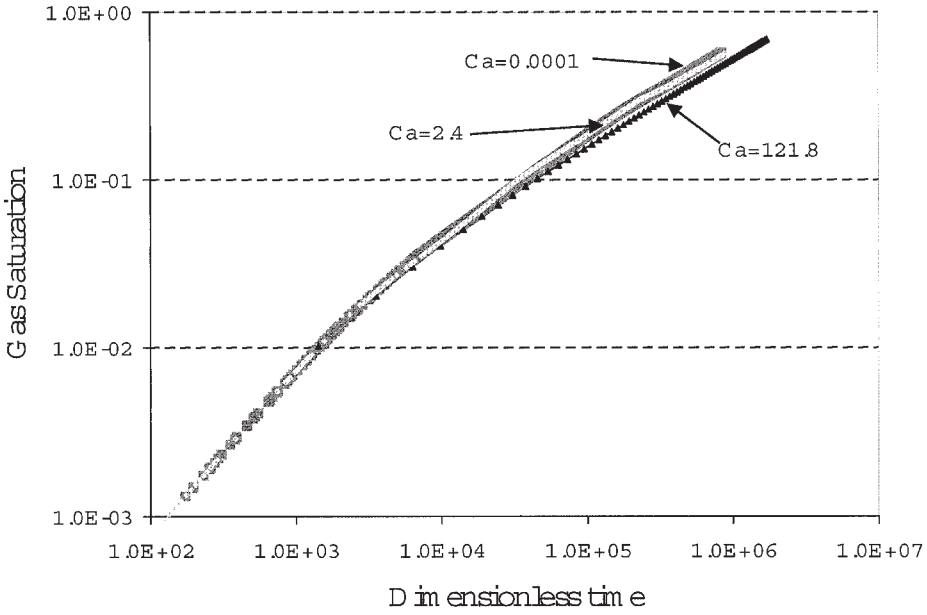

Figure 10. Dimensionless drying curve (gas saturation) as a function of the dimensionless time, for three different values of the capillary number.

The large-Ca limit coincides with the expected scaling behavior $t^{0.5}$.

$$\zeta = 1 + \frac{A}{C_0} x \tag{32}$$

whereas the film radius obeys the quasi-static Laplace equation

$$\nabla^2 \rho^3 = 0 \tag{33}$$

At the percolation boundary P, the latter is constant, $\rho = 1$. In the dry region G, films are absent, $\rho = 0$, and the concentration obeys the quasi-static diffusion equation

$$\nabla^2 \zeta = 0 \tag{34}$$

with boundary condition $\zeta = 0$ at the open end. In contrast to the previous, however, the evaporation interface cannot be explicitly calculated. Rather, it is at the location $x = x_f(y, t)$, given implicitly from the solution of the two equations

$$\zeta = 1 + \frac{A}{C_0} x_f(y, t) \tag{35}$$

$$\frac{1}{\mathrm{Ca}_0} \frac{\partial \rho^3}{\partial n} = \frac{\partial \zeta}{\partial n} \tag{36}$$

the latter expressing conservation of mass at the front. In the above, the capillary number is based on the reference equilibrium concentration C_0.

Because of the dependency of the front location on the transverse coordinate y, the solution of this problem does not benefit from the previous transformation and must be solved iteratively, as follows. First, the front location is guessed, and the two Laplace Eqs. 33 and 34 are solved as boundary value problems in their respective regions. The mass balance at the front, Eq. 36 is then used to check the accuracy of the initial guess and iteration is applied until convergence is reached. This approach was implemented in the results shown below. Before we proceed further, however, it is instructive to consider two special cases:

(1) At small capillary numbers, the problem can be further simplified. From our previous experience, the film front in such cases is far enough from the percolation front, so that it can be assumed flat, without great loss. In this case, therefore, the problem can be solved by applying iteration, but only on the average front location. In addition, by assuming that $x \approx x_f(t)$, then we can use the transformation of the isothermal case and define the auxiliary variable

$$\Phi = \frac{\rho^3 + \mathrm{Ca}_0 \zeta}{1 + \mathrm{Ca}_0 \left[\frac{A}{C_0} x_f(t) + 1 \right]} \tag{37}$$

This variable satisfies the Laplace equation everywhere, it is continuous and with continuous derivatives everywhere, and it is subject to the boundary conditions $\Phi = 1$ at the percolation front and $\Phi = 0$ at the open boundary. Its solution, $\Phi(x, y)$, is obtained in a straightforward manner, as before. Now, the location of the evaporation front $x_f(t)$ is the contour at which

$$\bar{\Phi}[x_f(t)] = \frac{\mathrm{Ca}_0 \left[\frac{A}{C_0} x_f(t) + 1 \right]}{1 + \mathrm{Ca}_0 \left[\frac{A}{C_0} x_f(t) + 1 \right]} \tag{38}$$

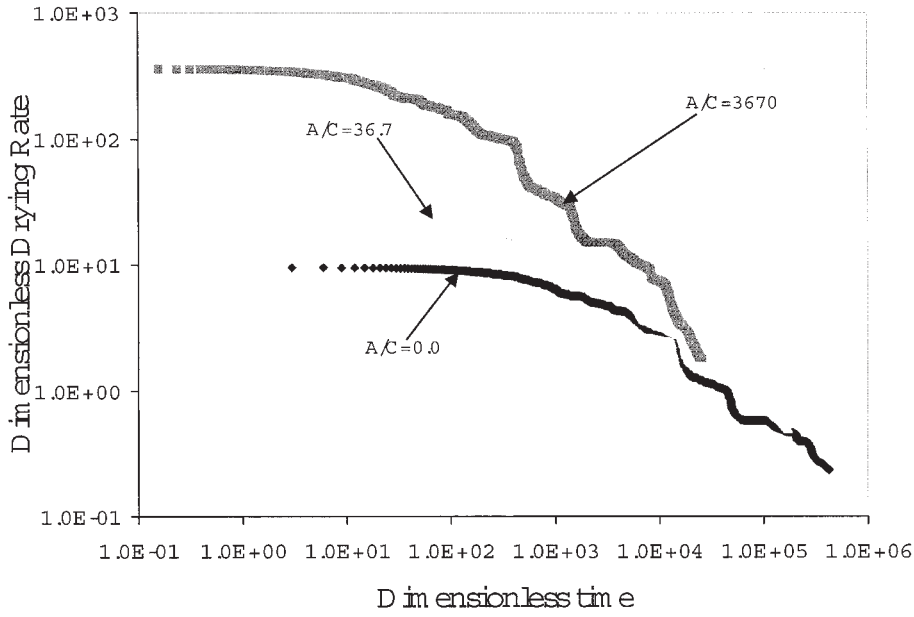

Figure 11. Effect of temperature gradients on the drying rates.

$Ca_0 = 10^{-4}$, $N = 100$.

where the bar denotes transverse average. Equation 38 is essentially an algebraic equation for x_f and requires an iterative solution, using the Laplace equation.

(2) An instructive illustration is possible for 1-D geometries. If we denote the location of the bulk liquid (percolation) front by x_p we have the solution

$$\Phi = \frac{N - x}{N - x_p} \tag{39}$$

It is not difficult to show, then, that the film tip location is the solution of the following quadratic equation

$$Ca_f^2 + (1 - Ca_p)Ca_f - Ca_N = 0 \tag{40}$$

where subscripts f, p, and N refer to the film tip, the liquid front, and the position of the open end, respectively. If the two capillary numbers at the ends are small or large, so is Ca_f, respectively.

The most interesting case is if Ca_p is small, but Ca_N is large, so that the solution of Eq. 40 is

$$Ca_f \approx \frac{-1 + \sqrt{1 + 4Ca_N}}{2} \approx Ca_N \tag{41}$$

indicating short films and the approach to the case discussed by Huinink et al. (2002).

The above methodology (iterative solution of Eqs. 35 and 36) was used to derive drying rate curves for the case when IP conditions at the front apply. As previously, the drying rate is

$$\Im = \frac{\phi WDlC_0}{Ca_0}(1 + Ca_f)\Im_D \tag{42}$$

where $\Im_D = -\int_{a_0} (\partial\Phi/\partial n)da$, whereas the analogous dimensionless time increment is

$$\Delta\tau = \frac{(1 + Ca_0)\left(\frac{\pi^2 r_c}{16\alpha l\phi}\right)}{(1 + Ca_f)\Im_D} \tag{43}$$

Results are shown in Figure 11, as a function of the parameter A/C_0. In these the dimensionless time was expressed in terms of the reference capillary number

$$t^* = \left(\frac{16\alpha}{\pi^2}\right)\left(\frac{V_p\rho_l}{r_c DC_{e0}}\right)\left(\frac{Ca_0}{1 + Ca_0}\right)$$

As expected, drying accelerates as the applied temperature gradient increases, particularly at early times. However, the effect is significant only if parameter A/C_0 is large. The temperature effect enters in both the dimensionless rate $\Im_D$ and in Ca_f in the combination $(1 + Ca_f)$. However, both from simulations, as well as from the simpler 1-D analysis above, the most important effect turns out to be the latter. In essence, the temperature gradient effect enters in ways similar to the effect of viscous forces in the bulk, in that it dominates only if Ca_f is of order 1. Thus, $(A/C_0)N$ must be quite large for a nontrivial effect to be felt. Figure 11 shows that this indeed the case. This effect diminishes at larger times, and all curves approach the same asymptote. We conclude that when film flow effects are dominant, nonisothermal effects are not important. On the other hand, for sufficiently strong temperature gradients, the films are short, nonisothermal effects becomes important, and the problem approaches the case discussed in Huinink et al. (2002).

Conclusions

This article has reported the investigation of the effect of capillarity-driven viscous flow through macroscopic liquid films during the isothermal drying of porous materials. A mathematical model that accounts for viscous flow in a 2-D pore network, through both the liquid films and the bulk liquid phase, was presented. Using a novel transformation, it was found that film flow is a major transport mechanism, its effect being dominant when capillarity controls the process, which is the case in typical applications. The effect of the films is explained by the fact that in their presence the gas phase remains saturated; little or no evaporation occurs in such pores; and the transport of the fluid is through strong capillary flow, which is effective in transporting the fluid closer to the open end, where larger concentration gradients exist. The extent of the films increases with a decrease in a suitably defined capillary number, where the driving force is diffusion. By contrast, viscous flow in the bulk contributes negligibly, for typical values, and becomes important in affecting patterns, but not rates, only at values of the capillary number of order 1. This result is different from that for external, forced drainage, where capillary number values of order of 10^{-3} are sufficiently large to affect displacement patterns. The difference is attributed to the counterflow mechanism of film flow. The results are in qualitative agreement with previous experimental work, which shows accelerated drying when films contribute to flow. Extension of the approach to nonisothermal conditions showed that if film flow dominates, temperature effects are secondary. The latter become strong only if films are short.

The approach we followed was subject to many assumptions. Evaporation was modeled in terms of simple diffusion-type processes, and detailed small-scale flow phenomena were ignored. Likewise, lumped into an effective diffusivity were transport effects near the open end of the medium. In addition, the variability of the pore microstructure was considered only in capillary properties, insofar as percolation patterns are concerned. In particular, the success of the mathematical transformation was based on ignoring heterogeneity in diffusive conductances for different pores. Finally, we have neglected the possibility of intercluster communication through films, by postulating that all films at the clusters have the same starting radius. We recognize that these are potentially important limitations that may preclude the precise quantitative comparison with experimental results. However, we believe that we have provided a good first approximation to the complicated problem of film flow in drying processes. It is also possible that the approach presented may find applications to other processes in porous media involving film flow, such as countercurrent imbibition.

Literature Cited

Blunt, M. J., M. D. Jackson, M. Piri, and P. H. Valvante, "Detailed Physics, Predictive Capabilities and Macroscopic Consequences for Pore-Network Models of Multiphase Flow," *Adv. Water Res.*, **25**, 1069 (2002).

Cazabat, A. M., F. Heslot, S. M. Troian, and P. Carles, "Fingering Instability of Thin Spreading Films Driven by Temperature Gradients," *Nature*, **346**, 824 (1990).

Chatzis, I., N. R. Morrow, and H. T. Lim, "Magnitude and Detailed Structure of Residual Oil Saturation," *SPE J.*, **23**, 311 (1983).

Constandinides, G. N., and A. C. Payatakes, "Effects of Precursor Wetting Films in Immiscible Displacement through Porous Media," *Transport Porous Media*, **38**, 291 (2000).

Davis, H. T., *Statistical Mechanics of Phases, Interfaces and Thin Films*, Wiley–VCH, New York (1996).

De Freitas, D. S., and M. Prat, "Pore Network Simulation of Evaporation of a Binary Liquid from a Capillary Porous Medium," *Transport Porous Media*, **40**, 1 (2000).

De Gennes, P. G., *Physics of Disordered Materials*, D. Adler, H. Fritzche, and S. R. Ovinsci, eds., Plenum Press, New York (1985a).

De Gennes, P. G., "Wetting: Statics and Dynamics," *Rev. Mod. Phys.*, **57**, 827 (1985b).

Derjaguin, B. V., N. V. Churaev, and V. M. Muller, *Surface Forces*, Consultants Bureau, New York (1987).

Dias, M. M., and A. C. Payatakes, "Network Models for Two-Phase Flow in Porous Media. Part I. Immiscible Microdisplacement of Non-Wetting Fluids," *J. Fluid Mech.*, **164**, 305 (1986).

Dillard, L. A., and M. J. Blunt, "Development of a Pore Network Simulation Model to Study Nonaqueous Phase Liquid Distribution," *Water Resources Res.*, **36**, 439 (2000).

Dong, M., and I. Chatzis, "The Imbibition and Flow of a Wetting Liquid along the Corners of a Square Capillary Tube," *J. Colloid Interface Sci.*, **172**, 278 (1995).

Dullien, A. L., C. Zarcone, I. F. MacDonald, A. Collins, and D. E. Bochard, "The Effects of Surface Roughness on the Capillary Pressure Curves and the Heights of Capillary Rise in Glass Bead Packs," *J. Colloid Interface Sci.*, **127**, 362 (1989).

Huinink, H. P., L. Pel, M. A. J. Michels, and M. Prat, "Drying Processes in the Presence of Temperature Gradients. Pore-Scale Modeling," *Eur. Phys. J. E*, **9**, 487 (2002).

Kataoka, D. E., and S. M. Troian, "A Theoretical Study of Instabilities at the Advancing Front of Thermally Driven Coating Films," *J. Colloid Interface Sci.*, **192**, 350 (1997).

Larson, R. G., L. E. Scriven, and H. T. Davis, "Percolation Theory of Residual Phases in Porous Media," *Nature*, **268**, 409 (1977).

Laurindo, J. B., and M. Prat, "Numerical and Experimental Network Study of Evaporation in Capillary Porous Media. Phase Distributions," *Chem. Eng. Sci.*, **51**, 5171 (1996).

Laurindo, J. B., and M. Prat, "Numerical and Experimental Network Study of Evaporation in Capillary Porous Media. Drying Rates," *Chem. Eng. Sci.*, **53**, 2257 (1998a).

Laurindo, J. B., and M. Prat, "Modeling of Drying in Capillary Porous Media: A Discrete Approach," *Drying Technol.*, **16**, 1769 (1998b).

Le Bray, Y., and M. Prat, "Three-Dimensional Pore Network Simulation of Drying in Capillary Porous Media," *Int. J. Heat Mass Transfer*, **42**, 4207 (1999).

Lenormand, R., "Liquids in Porous Media," *J. Phys. Condens. Matter*, 2, SA79 (1992).

Lenormand, R., and C. Zarcone, "Role of Roughness and Edges during Imbibition in Square Capillaries," *SPE J.*, 13264 (1984).

Lenormand, R., and C. Zarcone, "Invasion Percolation in an Etched Network: Measurement of a Fractal Dimension," *Phys. Rev. Lett.*, **54**, 2226 (1985).

Li, X., and Y. C. Yortsos, "Theory of Multiple Bubble Growth in Porous Media by Solute Diffusion," *Chem. Eng. Sci.*, **50**, 1247 (1995).

Luikov, A. V., *Heat and Mass Transfer in Capillary Porous Media*, Pergamon Press, London (1966).

Nowicki, S. C., H. T. Davis, and L. E. Scriven, "Microscopic Determination of Transport Parameters in Drying Porous Media," *Drying Technol.*, **10**, 925 (1992).

Oron, A., Davis, S. H. and S. G. Bankoff, "Long-Scale Evolution of Thin Liquid Films," *Rev. Mod. Phys.*, **69**, 931 (1997).

Pan, S. X., H. T. Davis, and L. E. Scriven, "Modeling Moisture Distribution and Binder Migration in Drying Paper Coating," *Tappi J.*, **78**, 127 (1995).

Peitgen, H.-M., and D. Saupe, eds., *The Science of Fractal Images*, Springer-Verlag, Berlin/New York (1988).

Peterson, G. P., *An Introduction to Heat Pipes: Modeling, Testing and Applications*, Wiley, New York (1994).

Plourde, F., and M. Prat, "Pore Network Simulations of Drying of Capillary Porous Media. Influence of Thermal Gradients," *Int. J. Heat Mass Transfer*, **46**, 1293 (2003).

Prat, M., "Percolation Model of Drying under Isothermal Condition in Porous Media," *Int. J. Multiphase Flow*, **19**, 691 (1993a).

Prat, M., "Isothermal Drying of Non-Hygroscopic Capillary Porous Materials as an Invasion Percolation Process," *Int. J. Multiphase Flow*, **21**, 875 (1993b).

Prat, M., "Recent Advances in Pore-Scale Models for Drying in Porous Media," *Chem. Eng. J.*, **86**, 153 (2002).
Prat, M., and B. Bouleux, "Drying of Capillary Porous Media With a Stabilized Front in Two Dimensions," *Phys. Rev. E*, **60**, 5647 (1999).
Ransohoff, T. C., and C. J. Radke, "Laminar Flow of a Wetting Liquid Along the Corners of a Predominantly Gas-Occupied Noncircular Pore," *J. Colloid Interface Sci.*, **121**, 392 (1988).
Rogers, J. R., and M. Kaviany, "Variation of Heat and Mass Transfer Coefficients During Drying of Granular Solids," *ASME J. Heat Transfer*, **112**, 668 (1990).
Satik, C., X. Li, and Y. C. Yortsos, "Scaling of Single-Bubble Growth in a Porous Medium," *Phys. Rev. E*, **51**, 3286 (1995).
Shaw, T. M., "Drying as an Immiscible Displacement Process with Fluid Counterflow," *Phys. Rev. Lett.*, **59**, 1671 (1987).
Stauffer, D., *Introduction to Percolation Theory*, Taylor & Francis, London (1985).
Tao, Y.-X., and M. Kaviany, "Simultaneous Heat and Mass Transfer from a Two-Dimensional Partially Liquid Covered Surface," *ASME J. Heat Transfer*, **113**, 874 (1991).
Toledo, P. G., H. T. Davis, and L. E. Scriven, "Fluids in Fractal Porous Media. Scaling of Transport Properties," *Physica A*, **185**, 228 (1992).
Tsimpanogiannis, I. N., Y. C. Yortsos, S. Poulou, N. Kanellopoulos, and A. K. Stubos, "Scaling Theory of Drying in Porous Media," *Phys. Rev. E*, **59**, 4353 (1999).
Vizika, O., and A. C. Payatakes, "Parametric Experimental Study of Forced Imbibition in Porous Media," *Physicochem. Hydrodyn.*, **11**, 187 (1989).
Wayner, P. C., "The Effect of Interfacial Mass Transport on Flow of Thin Liquid Films," *Colloids Surf.*, **52**, 71 (1991).
Wayner, P. C., "Intermolecular Forces in Phase-Change Heat Transfer: 1998 Kern Award Review," *AICHE J.*, **45**, 2055 (1999).
Whitaker, S., "Simultaneous Heat, Mass and Momentum Transfer in Porous Media. A Theory of Drying," *Adv. Heat Transfer*, **1**, 23 (1977).
Whitaker, S., "Coupled Transport in Multiphase Systems. A Theory of Drying," *Adv. Heat Transfer*, **13**, 1 (1998).
Whitaker, S., *The Method of Volume Averaging*, Kluwer Academic, Dordrecht, The Netherlands (1999).
Wilkinson, D., "Percolation Model of Immiscible Displacement in the Presence of Buoyancy Forces," *Phys. Rev. A.* **30**, 520 (1984).
Wilkinson, D., "Percolation Effects in Immiscible Displacement," *Phys. Rev. A*, **34**, 1380 (1986).
Wilkinson, D., and J. F. Willemsen, "Invasion Percolation: A New Form of Percolation Theory," *J. Phys. A*, **16**, 3365 (1983).
Witten, T. A., and L. M. Sander, "Diffusion-Limited Aggregation. A Kinetic Critical Phenomenon," *Phys. Rev. Lett.*, **47**, 1400 (1981).
Xu, B., Y. C. Yortsos, and D. Salin, "Invasion Percolation with Viscous Forces," *Phys. Rev. E*, **57**, 739 (1998).
Yiotis, A. G., A. K. Stubos, A. G. Boudouvis, I. N. Tsimpanogiannis, and Y. C. Yortsos, "The Effect of Liquid Films on the Isothermal Drying of Porous Media," *Phys. Rev. E*, **68**, 037303 (2003).
Yiotis, A. G., A. K. Stubos, A. G. Boudouvis, and Y. C. Yortsos, "A 2-D Pore-Network Model of the Drying of Single-Component Liquids in Porous Media," *Adv. Water Res.*, **24**, 439 (2001).
Yortsos, Y. C., and A. K. Stubos, "Phase Change in Porous Media," *Curr. Opin. Colloid Interface Sci.*, **6**, 208 (2001).
Zhou, D., M. Blunt, and Orr, F. M. Jr., "Hydrocarbon Drainage along Corners of Noncircular Capillaries," *J. Colloid Interface Sci.*, **187**, 11 (1997).

Appendix A

Steady-state single-capillary film flow

We can demonstrate the conjectures regarding the approach to steady state of Eqs. 9 and 11 by considering the numerical solution of an initial-boundary value problem involving a film exposed to a dry environment at one end, with film thickness and mass flux through the film specified at the origin, and with an insulating boundary for the gas mass flux at the origin. Thus, we take initial conditions $\zeta = 1$ at $t = 0$, boundary conditions $\rho = 1$ and $(\partial\rho/\partial\xi) = -(2\text{Ca}/\pi)$ at $\xi = 0$, and the constraint $\zeta = 0$ at the open end. The initial condition for the film radius was taken in the form shown below, which corresponds to an initial steady state of the problem but for a different origin of the liquid. The problem solved essentially corresponds to the case where the origin suddenly recedes. The solution of the coupled equations was obtained using a finite-differences scheme. Results for the rescaled thickness are shown in Figure A1 as a function of distance and time. For the parameters of the figures after a time of about 20τ a steady state is reached.

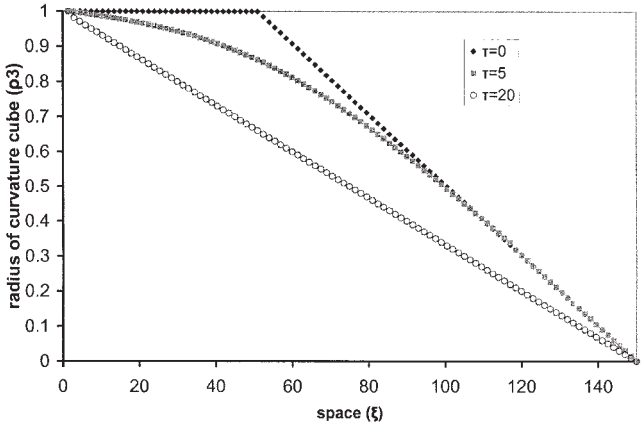

Figure A1. Approach to steady state of the rescaled thickness in a single capillary as a function of time and space.
$\text{Ca} = 10^{-5}$.

Appendix B

Film thickness at the liquid cluster perimeter

A key assumption made throughout the text was that the film radius at the liquid clusters, both CC and DC, remains constant and equal to r_c, corresponding to the percolation threshold, the notion being that, at least under IP conditions, the process is always at the percolation threshold. There is a flaw with this approximation, however.

Although at IP conditions, the pore throat radius being invaded does not remain constant, because of the invasion nature of the process, but rather varies randomly, between the largest throat value of the distribution and r_c. Allowing for such variation is possible, by setting the current value of the film radius to correspond to the largest value of the perimeter throat of the given cluster. Then, the value of Φ at the front would be

$$\Phi = \frac{\left(\frac{r_i}{r_0}\right)^3 + \text{Ca}}{1 + \text{Ca}} \tag{B1}$$

where r_i is the currently largest value of the throat at each cluster. Now, the DCs ahead of the CC will have on average smaller values of Φ, given that their currently largest throat radii are likely to be smaller. As a result, there is potentially net liquid flow from the CC to the DC through films that will connect the two clusters.

Figure B1 shows the drying curve (plotted vs. the dimensionless time in a semilog plot) for two different pore-throat size distributions, one corresponding to a wide (0.017–0.027)

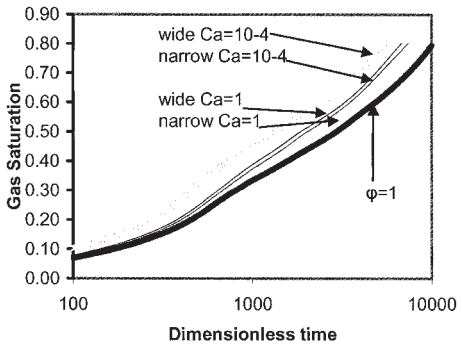

Figure B1. Drying curves vs. dimensionless time plotted in a semilog plot for two different values of the capillary number and two different throat size distributions.

Also shown is the case of a unimodal size distribution.

and another to a narrow (0.021–0.023) throat distribution and for two different values of Ca. Note that because Φ is not constant any longer, the problem must be solved separately for different values of Ca. As expected, the wide distribution leads to faster drying rates because the gradient of Φ is on average larger, whereas both curves are higher than the case in the text, where $\Phi = 1$. (It must be also noted that because Φ is not constant over the liquid cluster perimeter, the isopotential contours are now different. In addition, there is the potential that net flow of liquid drains from the CC to one or more of the DCs. These phenomena will be detailed in a separate analysis.)

It is possible, however, to collapse all the curves, by redefining an effective radius r_c, which enters in the dimensional time, both directly and through the capillary number. For example, the two curves can collapse with each other and with the constant Φ case, in the semilog plot of Figure B1, by appropriate shifting of the time axis. In the low Ca case, from the amount of the shift, we can determine this effective r_c, by equating the shift with $\log r_c^2$, whereas in the case of large Ca, the shift is closer to $\log r_c$. With this procedure we find that the effective radii turn out to be the average between the maximum value of the distribution and the mean. We conclude that at least the drying curves can be well approximated with the constant Φ assumption, provided that an adjusted effective value for r_c is used.

Manuscript received Jul. 11, 2003, and revision received Mar. 2, 2004.